Electromagnetic contribution to surface-enhanced Raman scattering from rough metal surfaces: A transformation optics approach

Yu Luo, Alexandre Aubry,[*] and J. B. Pendry

The Blackett Laboratory, Department of Physics, Imperial College London, London SW7 2AZ, United Kingdom

The propagation of surface plasmons along rough metal surfaces is investigated with transformation optics. The roughness is modeled on a nanometer scale either by partly embedding a cylinder of metal into the surface (convex rough surface) or by excavating a cylindrical cavity from it (concave rough surface). These two structures can be treated analytically by means of conformal transformation. The interaction of surface plasmons with the singularities of these structures is shown to induce extreme field enhancements. These modes dominate the surface-enhanced Raman-scattering response and enhancement factors of the order of 10^7 are predicted. Interestingly, concave rough surfaces are shown to be the best candidates for surface-enhanced Raman scattering due to a stronger field enhancement and a lower sensitivity to the incident light polarization. Our analytical approach also points out the influence of the contact angle between the asperities and the metal surface on the bandwidth and the efficiency of the light-harvesting process.

PACS number(s): 78.68.+m, 73.20.Mf, 78.30.Er

I. INTRODUCTION

Surface-enhanced Raman scattering (SERS) corresponds to the significant enhancement (of up to 10^6) of Raman signals observed for molecules absorbed on specially prepared metal surfaces.[1–3] The SERS effect has been demonstrated experimentally in a number of noble metals such as copper, silver, and gold, either in the form of nanoparticles or with structured surfaces.[1–9] Although the basic physics behind SERS is not completely understood, the huge enhancements of Raman signals have been mainly attributed to two mechanisms, namely, a classical electromagnetic (EM) effect and a chemical effect. To a first-order approximation, the EM contribution to the Raman signal enhancement can be modeled as the fourth power of the total electric-field enhancement at the molecule position.[10] This fact has enabled a computational approach to SERS, where the interaction of light with metal surfaces is studied through an implementation of Maxwell's equations on adaptive meshes.[10] Since then, theoretical investigations of this problem have drawn considerable attention.[11–22] It is now generally agreed that the exotic EM enhancements in SERS experiments are primarily related to the strongly localized surface-plasmon modes induced by sharp surface protrusions or at interstices between nanoparticles.[10–12,15–20,22] Further quantitative understanding of such surface-plasmon modes is strongly dependent on theoretical advances in this area.

In the literature, theoretical investigations of the plasmonic structures used in SERS experiments have been mostly limited to numerical simulations. Analytical treatments have still remained a challenge, probably because the presence of sharp surface protrusions or other singularities makes the calculation more complex. Transformation optics[23,24] provides an elegant and powerful solution to this problem. The general strategy is as follows: start with a well-understood canonical plasmonic system whose analytical description is possible, and then apply a conformal transformation to deduce the solution for a much more complex geometry.[25] This concept was first deployed to design efficient light-harvesting devices[25] and then

extended to examine a general class of singular structures.[26] In Ref. 26, we have shown that singular plasmonic structures (such as metal surfaces with sharp edges or triangular crevices) generally exhibit a cutoff behavior and a divergent feature. However, the light-harvesting properties and the Raman-scattering responses of such singular structures have not been studied in detail.

This paper will focus on the interaction of surface-plasmon modes with two typical surface defeats that arise on rough metal surfaces. The first one is a cylindrical protrusion which is partly embedded in a metal surface [see Fig. 1(b1)], while the second one corresponds to a cylindrical groove engraved onto a planar metal surface [see Fig. 1(b2)]. In the following part of the paper, we shall refer to the structures depicted in Figs. 1(b1) and 1(b2) as the convex and concave rough surfaces, respectively. As we will see, a decisive parameter is the angle subtended at the apex [e.g., θ depicted in Figs. 1 (b1) and 1(b2)] which we will refer to as the contact angle between the asperities and the metal surface. The surface-plasmon dispersion in these two structures is shown to exhibit a lower bound cut-off frequency. Around this frequency, the compression of energy results in a dramatic increase of electric fields as surface plasmons propagate to the apexes of the structure. The corresponding surface-enhanced Raman-scattering response is thus highly localized in the vicinities of the apexes. On the contrary, close to the surface-plasmon frequency, the electric field vanishes in the vicinities of the two apexes due to the decrease of the surface-plasmon velocity and the increase of the dissipation losses. This gives rise to a considerable Raman signal enhancement (with a maximum up to 10^7 in some cases) which spreads over the whole metal surface. The influence of other parameters, such as the contact angle θ and the polarization of the incident light, will be also studied in detail. In particular, we will show that the concave rough surface induces a much larger Raman-scattering response and is more robust to the polarization of the incident light than a convex rough surface. A small contact angle between the asperities and the metal surface will be shown to greatly improve the bandwidth and the efficiency of the SERS
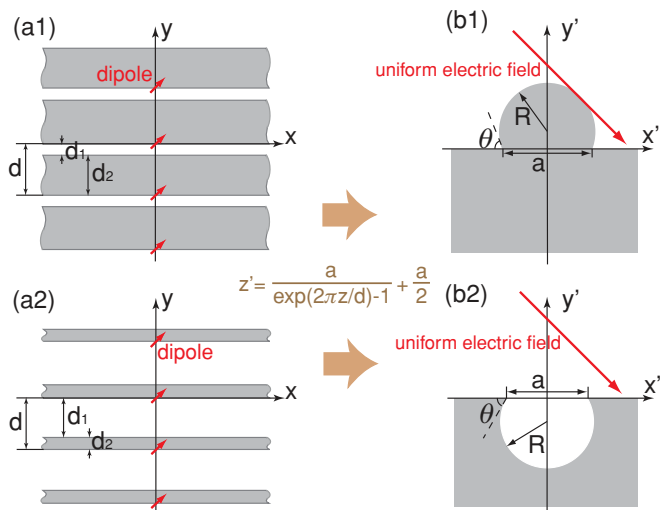
FIG. 1. (Color online) The schematic of transformation. (a1) and (a2) Periodic metallic slabs excited by a line dipole array, transporting SPPs to $x \rightarrow \pm\infty$. The thicknesses of each dielectric media and metallic slab are d_1 and d_2, respectively. In (a1) $d_1 < d_2$, while in (a2) $d_1 > d_2$. Under a conformal transformation described by Eq. (1), the convex (b1) and concave (b2) rough surfaces are obtained, and the line dipole array in (a1)/(a2) is mapped to a uniform electric field E'_{inc} in (b1)/(b2).

process. Such a broadband nature of the enhancement would be particularly important in SERS experiments since it would lead to an efficient concentration of the exciting radiation at the molecular site and an efficient collection of emitted radiation, even if emitted at a very different frequency.

The organization of this paper is as follows: in Sec. II, the transformation of geometries is first presented; then in Sec. III, the coupling of a dipole array to a periodic metallodielectric system (which is equivalent to the problem of convex/concave rough surfaces under plane-wave illumination) is discussed in detail; in Sec. IV, closed-form expressions of the field enhancement and of the power absorbed by convex/concave rough surfaces are derived analytically. The surface-plasmon modes responsible for SERS responses are investigated and the optical responses of the two structures are studied as a function of the contact angle θ; finally, a conclusion is drawn in Sec. V.

II. TRANSFORMATION OF GEOMETRIES

The original geometry is a line dipole array embedded in periodic metallic slabs, as shown in Figs. 1(a1) and 1(a2). Each metallic slab with a thickness d_2 is separated by a distance d_1 from the adjacent one. Each element of the line dipole array is located at the position $x = 0$, $y = md$ (where m is an arbitrary integer). These dipoles couple to the surface-plasmon polaritons (SPPs) supported by the surrounding metal slabs and transport their energy out to infinity. Now we apply the following conformal transformation:

$$z' = \frac{a}{\exp(2\pi z/d) - 1} + \frac{a}{2}, \quad (1)$$

where $z = x + iy$ and $z' = x' + iy'$ are the usual complex number notations. The configurations shown in Figs. 1(a1)

and 1(a2) are mapped to the convex [Fig. 1(b1)] and concave [Fig. 1(b2)] rough surfaces, respectively. In this process, two singularities are created at $z' = a/2$ and $z' = -a/2$ in the transformed geometry, corresponding to $x \rightarrow +\infty$ and $x \rightarrow -\infty$ in the original coordinate system. Therefore, similarly to the initial metallodielectric system which supports SPPs transporting the energy to infinity [Figs. 1(a1) and 1(a2)], the transformed structure [Figs. 1(b1) and 1(b2)] supports localized surface plasmons propagating toward the structure apexes (singularities) where energy accumulates.[25,26] The angle subtended at the apex, which will be referred to as the contact angle, is denoted as θ. It takes the following form:

$$\begin{aligned} \theta = 2\pi d_1/d, & \quad \text{when} \quad d_1 < d_2, \\ \theta = 2\pi d_2/d, & \quad \text{when} \quad d_1 > d_2, \end{aligned} \quad (2)$$

where $d = d_1 + d_2$. The radius of the embedded cylinder/extracted cavity shown in Figs. 1(b1) and 1(b2) is given by

$$R = \frac{a}{2\sin\theta}. \quad (3)$$

The transformation of the sources is equally important. The location of each dipole $z = imd$ is transformed to $z' = \infty$, indicating that the two charges comprising each element of the line dipole array in the original coordinate are also mapped to infinity. As pointed out in Ref. 25, these two charges (separated by an infinite distance) give rise to a uniform electric field in the transformed space. If each element of the dipole array in the z frame has a dipole moment $\overline{p} = p_x x + p_y y$, the incident electric field in the z' frame has a strength

$$\bar{E}'^{\text{inc}} = \frac{1}{\varepsilon_0 ad}(xp_x - yp_y). \quad (4)$$

When the dimensions of the structures are sufficiently small compared with the wavelength of the probe light (e.g., $R < 50$ nm), solving the Helmholtz equation $(\nabla'^2 + k^2)\phi' = 0$ (in the transformed space) is equivalent to solving the Laplace equation $\nabla'^2 \phi' = 0$. This indicates that the surface plasmon modes can be well described in the near-field approximation and the uniform electric field can be considered as an incident plane wave. In the case of two-dimensional conformal transformations, the permittivity of the material remains unchanged. The form invariance of the Laplace equations insures the preservation of the electrostatic potential $\phi(x,y) = \phi'(x',y')$, thus solving the problem in the original frame [Figs. 1(a1) and 1(a2)] will provide an analytical solution for the concave/convex rough surface problems [Figs. 1(b1) and 1(b2)].

III. COUPLING OF A LINE DIPOLE ARRAY TO PERIODIC METALLIC SLABS

To calculate the potential induced in the periodic metallodielectric structure, we first expand the incident potential of each dipole array element by a Fourier transform along the x direction:

$$\begin{aligned} \phi^{\text{inc}}(k) &= \int \phi^{\text{inc}}(x,y)e^{-ikx}\,dx \\ &= \frac{1}{2\pi\varepsilon_0}\int_{-\infty}^{\infty} \frac{xp_x + yp_y}{x^2 + y^2}e^{-ikx}\,dx = a(k)e^{-|ky|}, \quad (5) \end{aligned}$$

with

$$a(k) = \frac{p_y \, \mathrm{sgn}(y) - i p_x \, \mathrm{sgn}(k)}{2\varepsilon_0}. \tag{6}$$

$\mathrm{sgn}(\cdot)$ represents the sign function. Since the structure shown in Figs. 1(a1) and 1(a2) is completely periodic along the y direction, solving the potential in one period will give the solution in the whole space. Here, we focus on the period $-d < y < 0$ and write the potential in the dielectric medium ($-d_1 < y < 0$) and the metallic slab ($-d < y < -d_1$) as follows:

$$\phi^{\mathrm{sca}}(k) = b_-(k)e^{ikx+|k|y} + b_+(k)e^{ikx+|k|y}, \tag{7}$$

$$\phi^m(k) = c_-(k)e^{ikx+|k|y} + c_+(k)e^{ikx+|k|y}, \tag{8}$$

where $b_-(k)$ and $b_+(k)$ are the Fourier coefficients associated with the scattering potential, while $c_-(k)$ and $c_+(k)$ correspond

to the potential inside the metal. The boundary conditions at the metal/dielectric interface and the periodicity of the problem yield the following equations:

$$a(k)e^{-|k|d_1} + b_-(k)e^{-|k|d_1} + b_+(k)e^{|k|d_1}$$
$$= c_-(k)e^{-|k|d_1} + c_+(k)e^{|k|d_1}, \tag{9}$$

$$a(k)e^{-|k|d_1} + b_-(k)e^{-|k|d_1} - b_+(k)e^{|k|d_1}$$
$$= \varepsilon c_-(k)e^{-|k|d_1} - \varepsilon c_+(k)e^{|k|d_1}, \tag{10}$$

$$a(k) + b_-(k) + b_+(k) = c_- e^{-|k|d} + c_+ e^{|k|d}, \tag{11}$$

$$a(k) - b_-(k) + b_+(k) = -\varepsilon c_-(k)e^{-|k|d} + \varepsilon c_+(k)e^{|k|d}. \tag{12}$$

Then the four unknown coefficients can be determined by solving Eqs. (9)–(12):

$$b_-(k) = \frac{(1 - e^{|k|d}) + (e^{|k|d_1} - e^{|k|d_2})e^{|k|d_2 + 2\alpha} + (e^{2|k|d_2} - 1)e^{2|k|d_1 + \alpha}}{e^{2\alpha}(e^{|k|d_1} - e^{|k|d_2})^2 - (e^{|k|d} - 1)^2} a(k), \tag{13}$$

$$b_+(k) = \frac{(1 - e^{|k|d}) + (e^{|k|d_1} - e^{|k|d_2})e^{|k|d_2 + 2\alpha} + (e^{2|k|d_2} - 1)e^\alpha}{e^{2\alpha}(e^{|k|d_1} - e^{|k|d_2})^2 - (e^{|k|d} - 1)^2} a(k), \tag{14}$$

$$c_-(k) = \frac{2e^{|k|d}}{\varepsilon + 1} \frac{(1 - e^{|k|d}) + (e^{|k|d_2} - e^{|k|d_1})e^{|k|d_1 + \alpha}}{e^{2\alpha}(e^{|k|d_1} - e^{|k|d_2})^2 - (e^{|k|d} - 1)^2} a(k), \tag{15}$$

$$c_+(k) = \frac{2}{\varepsilon + 1} \frac{(1 - e^{|k|d}) + (e^{|k|d_2} - e^{|k|d_1})e^{-|k|d_1 + \alpha}}{e^{2\alpha}(e^{|k|d_1} - e^{|k|d_2})^2 - (e^{|k|d} - 1)^2} a(k), \tag{16}$$

where we have introduced a constant

$$\alpha = \begin{cases} \ln[(\varepsilon - 1)/(\varepsilon + 1)], & \text{when } \mathrm{Re}\{\varepsilon\} > -1 \\ \ln[(\varepsilon - 1)/(\varepsilon + 1)], & \text{when } \mathrm{Re}\{\varepsilon\} < -1. \end{cases} \tag{17}$$

Equations (13)–(16) indicate that the four unknown coefficients diverge under the same condition:

$$e^{2\alpha}(e^{|k|d_1} - e^{|k|d_2})^2 - (e^{|k|d} - 1)^2 = 0. \tag{18}$$

This is the dispersion relation of surface plasmons supported by periodic metallic slabs under the near-field approximation. Substituting the expressions of d_1 and d_2 [Eqs. (2)] into Eq. (18) yields

$$\sinh\left[\frac{(1 - \theta/\pi)|k|d}{2}\right] = e^{-\alpha} \sinh\left(\frac{|k|d}{2}\right). \tag{19}$$

Equation (19) indicates that $|k|d$ is a complex number uniquely determined by α and θ. Let us assume $|k|d = f(\alpha,\theta)$. Its exact value can be obtained by applying a computational recurrence method to Eq. (19). However, a simple closed form of $f(\alpha,\theta)$ is not available. In the following, we shall make some effort to find its approximate solution by considering the asymptotic limits of $f(\alpha,\theta)$ when $f(\alpha,\theta) \to 0$ and

$f(\alpha,\theta) \gg 1$.[27] A detailed calculation shows that to a first-order approximation, $f(\alpha,\theta)$ can be written as

$$f(\alpha,\theta) = \begin{cases} \frac{2\pi\alpha}{\theta}, & f(\alpha,\theta) \gg 1 \\ 2\sqrt{6}\sqrt{\frac{1 - (1 - \theta/\pi)e^\alpha}{1 - (1 - \theta/\pi)^3 e^\alpha - 1}}, & f(\alpha,\theta) \to 0. \end{cases} \tag{20}$$

In Fig. 2 we plot the exact value of $f(\alpha,\theta)$ (the blue solid line) as well as its large-scale approximation (the black dashed line) and small-scale approximation (the red dash-dotted line). Here the metal is assumed to be silver, with the permittivity taken from experimental data.[28] The agreement between the exact and approximate results indicates that by appropriately combining the small- and large-scale limits of $f(\alpha,\theta)$ (at the intersection point of the blue dashed line and red dashed-dotted line), an approximate closed-form solution can be obtained at any frequency. Interestingly, Fig. 2 also shows that surface-plasmon excitations in the periodic metallodielectric structure have a lower bound cutoff at a finite frequency ω_c and an upper bound cutoff below the bulk plasma frequency ω_p. This phenomenon is quite different from what happens in a single metallic slab, where the SPPs dispersion relation does not show any lower bound cutoff while an upper bound cutoff is expected at ω_p. Note that due to the relatively narrow band of the mode excited above the surface-plasmon frequency ω_{sp}, the upper bound is not prominent in Fig. 2.

The cutoff behavior can also be understood by taking the limit $k \to 0$ in Eq. (18), which yields

$$\left(\frac{d_1 + d_2}{d_1 - d_2}\right)^2 = \left(\frac{\varepsilon - 1}{\varepsilon + 1}\right)^2. \tag{21}$$

The lower bound cutoff frequency ω_c and upper bound cutoff frequency ω'_c can then be determined through a simplification of Eq. (21),

$$\varepsilon(\omega_c) = \frac{1}{\varepsilon(\omega'_c)} = -\frac{\max\{d_1, d_2\}}{\min\{d_1, d_2\}}, \tag{22}$$

where $\varepsilon(\omega_c)$ and $\varepsilon(\omega'_c)$ are the permittivity of the metal at ω_c and ω'_c, respectively. When $d_1 \gg d_2$ (or $d_1 \ll d_2$), the periodic metallodielectric structure is equivalent to a single metallic slab (or two semi-infinite metal surfaces separated by a thin dielectric film). In this case, Eq. (22) is reduced to $\varepsilon(\omega_c) \to -\infty$ and $\varepsilon(\omega'_c) \to 0$, indicating that the lower bound cutoff occurs at zero frequency ($\omega_c = 0$) and the upper bound cutoff occurs at the bulk plasma frequency ($\omega'_c = \omega_p$).

Now that we have solved the problem in k space, the induced potentials can then be deduced in the real space by applying an inverse Fourier transform to Eqs. (7) and (8):

$$\phi^{\text{sca}}(x,y) = \frac{1}{2\pi} \int [b_-(k)e^{|k|y} + b_+(k)e^{-|k|y}]e^{ikx} \, dk, \tag{23}$$

$$\phi^m(x,y) = \frac{1}{2\pi} \int [c_-(k)e^{|k|y} + c_+(k)e^{-|k|y}]e^{ikx} \, dk. \tag{24}$$

To perform the integrals in Eqs. (23) and (24), we have to evaluate the poles in the integrand and a cut which runs from $k = 0$ to either $k = +i\infty$ or $k = -i\infty$.[29] The poles are related to the excitation of propagating surface plasmons, while the cut is associated with lossy surface waves, which dissipate no energy if ε is real.[30] Since the SPPs excitation above the surface-plasmon frequency ω_{sp} is relatively narrow band (e.g., Fig. 2 shows that the bandwidth of this mode is smaller than 40 THz for silver), we shall focus on the frequency range below ω_{sp} in the following discussions. In this case, the imaginary part of ε is relatively small compared with the real part. Thus, we can neglect the contribution from the cut and only evaluate the contribution of the poles in $b_-(k)$, $b_+(k)$, $c_-(k)$, and $c_+(k)$. It is worth pointing out that the sum of the residues of the poles diverges at the point $x = 0$, $y = 0$, indicating that the electric field is infinite at the dipole position. In the rest of the space, the integrals in Eqs. (23) and (24) are dominated by the pole with the smallest imaginary part. A detailed calculation shows that when $x^2 + y^2 \neq 0$ the induced potentials in the real space take the following form:

$$\phi^{\text{sca}}(x,y) = -\frac{1}{4\varepsilon_0 d} \left[[i\Gamma_y p_y + \text{sgn}(x)\Gamma_x P_x]e^{f(\alpha,\theta)y/d} + [i\Lambda_y p_y + \text{sgn}(x)\Lambda_x P_x]e^{-f(\alpha,\theta)y/d} \right] e^{if(\alpha,\theta)|x|/d}, \tag{25}$$

$$\phi^m(x,y) = -\frac{1}{2\varepsilon_0(\varepsilon+1)d} \left[[i\Theta_y p_y + \text{sgn}(x)\Theta_x p_x]e^{f(\alpha,\theta)y/d} + [i\Omega_y p_y + \text{sgn}(x)\Omega_x p_x]e^{-f(\alpha,\theta)y/d} \right] e^{if(\alpha,\theta)|x|/d}, \tag{26}$$

where

$$\Gamma_x = \frac{d[e^{\alpha+2f(\alpha,\theta)(d_1+d_2)/d} - e^{\alpha+2f(\alpha,\theta)d_1/d} - e^{2\alpha+2f(\alpha,\theta)d_2/d} + (e^{2\alpha}-1)e^{f(\alpha,\theta)} + 1]}{(e^{f(\alpha,\theta)}-1)[e^\alpha(d_1e^{f(\alpha,\theta)d_1/d} - d_2e^{f(\alpha,\theta)d_2/d})\text{sgn}(d_1-d_2) - de^{f(\alpha,\theta)}]},$$

$$\Gamma_y = \frac{d[e^{\alpha+2f(\alpha,\theta)(d_1+d_2)/d} - e^{\alpha+2f(\alpha,\theta)d_1/d} + e^{2\alpha+2f(\alpha,\theta)d_2/d} - (e^{2\alpha}-1)e^{f(\alpha,\theta)} - 1]}{(e^{f(\alpha,\theta)}-1)[e^\alpha(d_1e^{f(\alpha,\theta)d_1/d} - d_2e^{f(\alpha,\theta)d_2/d})\text{sgn}(d_1-d_2) - de^{f(\alpha,\theta)}]},$$

$$\Lambda_x = \frac{d[(e^{\alpha+2f(\alpha,\theta)d_2/d} + 1)(1 - e^\alpha) + (e^{2\alpha}-1)e^{f(\alpha,\theta)}]}{(e^{f(\alpha,\theta)}-1)[e^\alpha(d_1e^{f(\alpha,\theta)d_1/d} - d_2e^{f(\alpha,\theta)d_2/d})\text{sgn}(d_1-d_2) - de^{f(\alpha,\theta)}]},$$

$$\Lambda_y = \frac{-d[(e^{\alpha+2f(\alpha,\theta)d_2/d} - 1)(1 + e^\alpha) - (e^{2\alpha}-1)e^{f(\alpha,\theta)}]}{(e^{f(\alpha,\theta)}-1)[e^\alpha(d_1e^{f(\alpha,\theta)d_1/d} - d_2e^{f(\alpha,\theta)d_2/d})\text{sgn}(d_1-d_2) - de^{f(\alpha,\theta)}]},$$

$$\Theta_x = \frac{d[(e^\alpha - 1)e^{f(\alpha,\theta)} - e^{\alpha+2f(\alpha,\theta)d_1/d} + 1]}{(e^{f(\alpha,\theta)}-1)[e^\alpha(d_1e^{f(\alpha,\theta)d_1/d} - d_2e^{f(\alpha,\theta)d_2/d})\text{sgn}(d_1-d_2) - de^{f(\alpha,\theta)}]},$$

$$\Theta_x = \frac{d[(e^\alpha + 1)e^{f(\alpha,\theta)} - e^{\alpha+2f(\alpha,\theta)d_1/d} - 1]}{(e^{f(\alpha,\theta)}-1)[e^\alpha(d_1e^{f(\alpha,\theta)d_1/d} - d_2e^{f(\alpha,\theta)d_2/d})\text{sgn}(d_1-d_2) - de^{f(\alpha,\theta)}]},$$

$$\Omega_x = \frac{d[1 - e^{f(\alpha,\theta)} + e^{\alpha+f(\alpha,\theta)(d_2-d_1)/d} - e^\alpha]}{(e^{f(\alpha,\theta)}-1)[e^\alpha(d_1e^{f(\alpha,\theta)d_1/d} - d_2e^{f_{\varepsilon,\theta}d_2/d})\text{sgn}(d_1-d_2) - de^{f(\alpha,\theta)}]},$$

$$\Omega_y = \frac{d[1 - e^{f(\alpha,\theta)} - e^{\alpha+f(\alpha,\theta)(d_2-d_1)/d} + e^\alpha]}{(e^{f(\alpha,\theta)}-1)[e^\alpha(d_1e^{f(\alpha,\theta)d_1/d} - d_2e^{f(\alpha,\theta)d_2/d})\text{sgn}(d_1-d_2) - de^{f(\alpha,\theta)}]}.$$
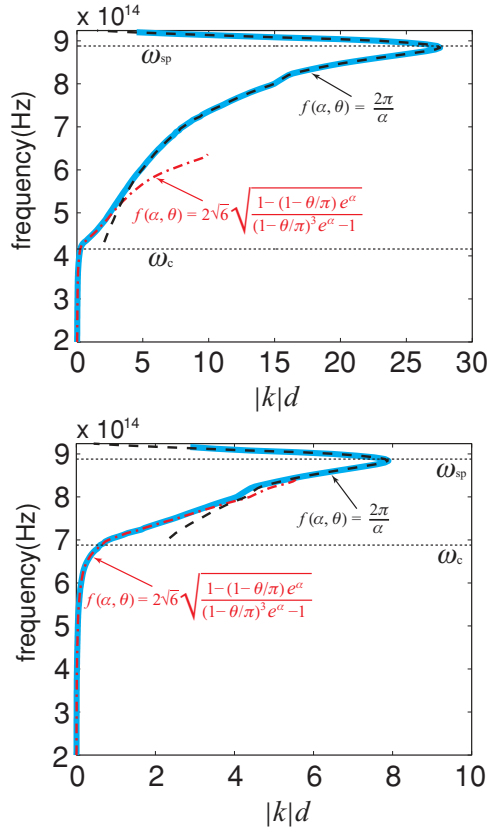
FIG. 2. (Color online) The dispersion relation of SPPs supported by the periodic metallodielectric structure for $d_1/d_2 = 20$ (upper panel) and $d_1/d_2 = 5$ (bottom panel). In both figures, the blue solid line corresponds to the exact solution to Eq. (19) using a computational recurrence method,[26] while the black dashed line and the red dash-dotted line are the large-scale and the small-scale approximation of $f(a,\theta)$, respectively. Here, the metal is assumed to be silver, with the permittivity taken from Palik's experimental data.[27] The two frequencies ω_c and ω_{sp} depicted in the figures represent the cutoff frequency and the surface-plasmon frequency, respectively.

Now that the solution to the original metallodielectric structure is obtained, the problem can be solved in the transformed space.

IV. SOLUTION TO THE TRANSFORMED STRUCTURES

A. The cutoff and divergent features

From the induced potential obtained in Sec. III, we can study the convex/concave rough surface in the transformed geometry. As pointed out in Ref. 26, singular plasmonic structures exhibit a cutoff behavior and a divergent feature. Here we first specify two characteristic frequencies for the structures shown in Figs. 1(b1) and 1(b2). The first one is the cutoff frequency ω_c (which is related to the cutoff behavior) and the second one is the critical frequency ω_0 (which is associated with the divergent feature).

The cutoff behavior has already been pointed out in the original frame. Replacing d_1 and d_2 by θ [Eq. (2)] into Eq. (22),
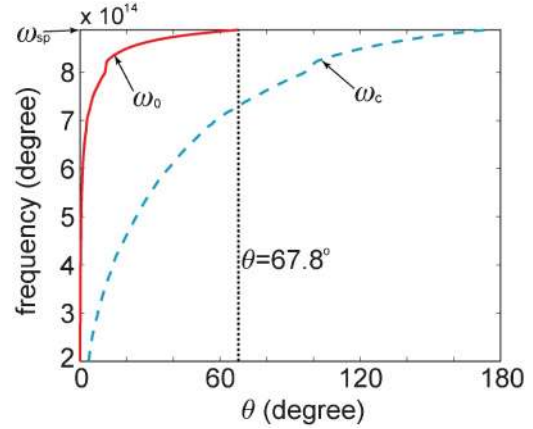

FIG. 3. (Color online) The dependence of ω_c and ω_0 on the contact angle θ.

one can show that the cutoff frequency ω_c only depends on the contact angle θ:

$$\varepsilon(\omega_c) = 1 - \frac{2\pi}{\theta}. \qquad (27)$$

The above relation of ω_c and θ is shown by the blue dashed line in Fig. 3. We can see that ω_c shows a blueshift as the angle θ increases. Therefore, a larger θ corresponds to a narrower frequency band. In particular, when $\theta = 180°$ (flat surface), all the surface-plasmon modes degenerate at the surface-plasmon frequency ω_{sp}.

The critical frequency ω_0 is defined as[26]

$$\text{Im} \left\{ \ln \left[\frac{\varepsilon(\omega_0) - 1}{\varepsilon(\omega_0) + 1} \right] \right\} = \theta. \qquad (28)$$

Beyond ω_0, the electric field vanishes as surface plasmons propagate toward the apexes of the structure, whereas below ω_0, the electric field diverges at the two apexes even when the metal is highly dissipative. Here, we should point out that the nonlocal properties of the permittivity encountered at small length scales[31,32] will also impair the divergence of the electric field. However, as long as we can fabricate the structures with very sharp apexes, the electric field can still be remarkably increased at the singularities. The red solid line in Fig. 3 shows the dependence of ω_0 on the angle θ. Similar to ω_c, ω_0 is found to increase with θ. And for any given angle θ, ω_0 is always larger than ω_c. It is worth pointing out that for silver,[28] ω_0 is equal to ω_{sp} at the angle $\theta = 67.8°$ and ω_0 only exists when $\theta \leqslant 67.8°$ [Eq. (28) is only valid for $\theta \leqslant 67.8°$]. Otherwise, a dramatic increase of the electric field is expected in the vicinities of the singularities over the whole spectrum.

B. Power absorbed by the convex/concave rough surface

We now consider the power absorbed by the convex/concave rough surface. Since the total energy is conserved under conformal transformations, the power absorbed by the transformed structures is equivalent to the power dissipated by the dipole in the original metallodielectric system. It can be calculated with the electric field (due to the excited surface-plasmon modes) backscattered at the dipole.[33] As it
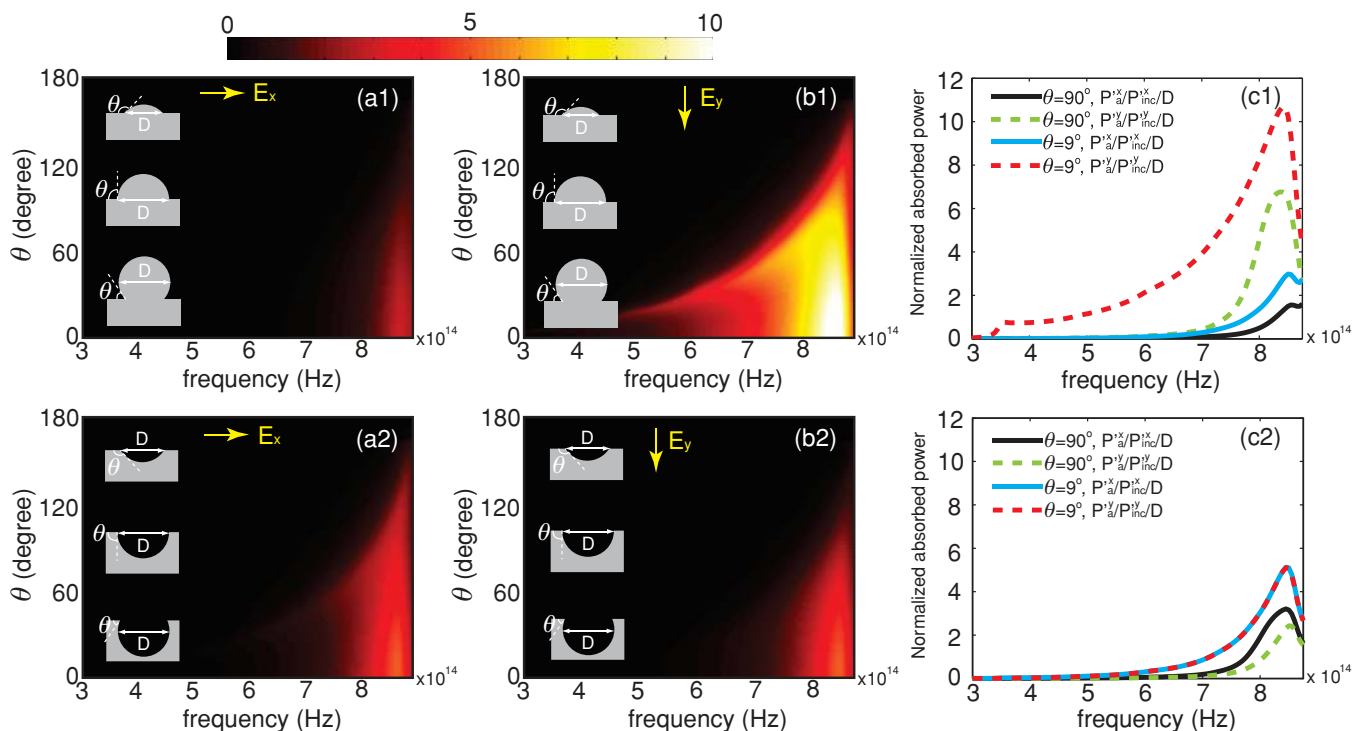
FIG. 4. (Color online) Normalized power absorbed by the convex (top panels) and concave (bottom panels) silver rough surfaces as a function of the contact angle θ and the frequency. (a1) and (a2) depict the case for the x-polarized illumination; (b1) and (b2) correspond to the y-polarized illumination. For the purpose of a clearer observation, we plot in (c1)/(c2) the normalized absorbed power as a function of the frequency for two specific contact angles ($\theta = 90°$ and $\theta = 9°$). Here the solid lines represent the x-polarized cases and the dashed lines correspond to the y-polarized cases.

has already been pointed out in Sec. III, this field diverges, indicating that the power absorbed by the whole convex/concave rough surface is infinitely large. However, since we are only

FIG. 5. (Color online) The real part of the normalized electric field $E'/E'^{\rm inc}$ for convex (upper panels) and concave (bottom panels) rough silver surfaces at $\omega = \omega_c = 810$ THz [(a1) and (a2)] and $\omega = \omega_{\rm sp} = 884$ THz [(b1) and (b2)]. Here the contact angle is $\theta = 90°$.

interested in the vicinity of the protuberance/indentation, the surface-plasmon mode propagating in this region is dominated by the pole with the smallest imaginary part. Thus, the power absorbed by the convex/concave rough surface in the small region around the protuberance/indentation is calculated as
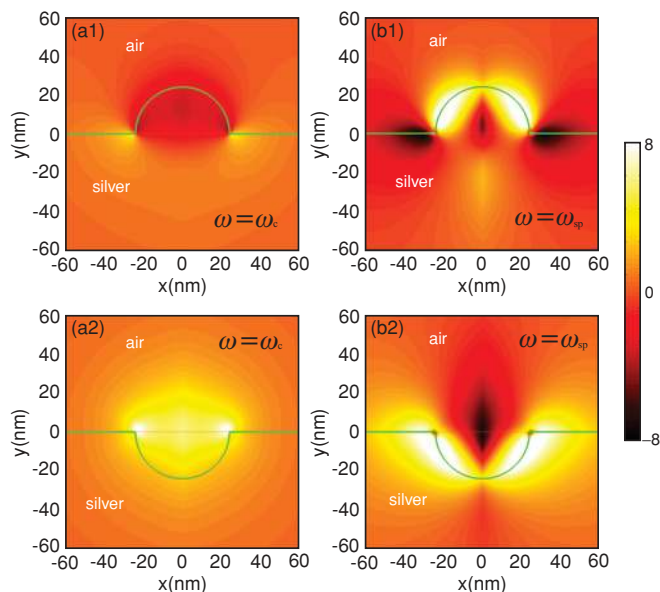
$$
\begin{aligned}
p'_a = p_d &= -\frac{\omega}{2}\mathrm{Im}\{\overline{p}^* \cdot \overline{E}(x=0, y=0)\} \\
&= \omega\,\mathrm{Re}\left[\frac{f(\alpha,\theta)(\Gamma_x + \Lambda_x)}{8\varepsilon_0 d^2}\right]p_x^2 \\
&\quad + \omega\,\mathrm{Re}\left[\frac{f(\alpha,\theta)(\Gamma_y + \Lambda_y)}{8\varepsilon_0 d^2}\right]p_y^2 \\
&= \frac{\varepsilon_0 a^2}{8}\mathrm{Re}[f(\alpha,\theta)(\Gamma_x + \Lambda_x)]\left|E'^{\rm inc}_x\right|^2 \\
&\quad + \frac{\varepsilon_0 a^2}{8}\mathrm{Re}[f(\alpha,\theta)(\Gamma_y + \Lambda_y)]\left|E'^{\rm inc}_y\right|^2. \quad (29)
\end{aligned}
$$

Renormalizing Eq. (29) by the incident power flux $P'_{\rm inc} = c\varepsilon_0|\overline{E}'^{\rm inc}|^2/2$, the power absorbed from an incident beam polarized along the x or the y axis can then be deduced:

$$
\begin{aligned}
\frac{P'^x_a}{P'^x_{\rm inc}} &= \frac{k_0 a^2}{4}\mathrm{Re}[f(\alpha,\theta)(\Gamma_x + \Lambda_x)], \\
\frac{P'^y_a a}{P'^y_{\rm inc}} &= \frac{k_0 a^2}{4}\mathrm{Re}[f(\alpha,\theta)(\Gamma_y + \Lambda_y)],
\end{aligned} \quad (30)
$$

where Γ_x, Γ_y, Λ_x, and Λ_y are constants defined in Sec III. $k_0 = \omega/c$ is the wave number in vacuum. Figure 4 displays the power absorbed by rough surfaces with different angles θ (or

different surface roughness). Here, the power is normalized by the characteristic dimension of the protuberance/indentation D ($D = a$ when $\theta \geqslant 90°$; $D = a/\sin\theta$ when $\theta < 90°$), as defined in the insets of Fig. 4. The metal is still assumed to be silver with the permittivity taken from Ref. 28.

The upper three panels of Fig. 4 show that the convex rough silver surface exhibits an anisotropic behavior: it shows a strong EM response to y-polarized illumination but a weak interaction with x-polarized incident fields. On the contrary, the concave rough silver surface interacts with x- and y-polarized fields with nearly equal strength, especially for small θ angle cases, as shown by the bottom three panels of Fig. 4.

Both the convex and concave rough silver surfaces exhibit a continuous absorption behavior over a broadband spectrum. This property originates from the fact that the group velocity of surface plasmons vanishes at the two apexes (singularities).[25] Hence, the surface plasmons are stopped at the singularities without being reflected, which prevents from any resonant feature. It is worth noticing that the presence of the singularities is decisive for the continuous absorption behavior. Otherwise,

the two structures tend to absorb light energy efficiently just at a few resonant frequencies, which is the case in nanoparticle dimers.[17–19,34–38] In addition, Fig. 3 shows that the power absorbed by the two structures increases as the angle θ decreases, and the maximum always occurs at the surface-plasmon frequency ω_{sp}.[26] In other words, the more pronounced the singularity is (small angle θ), the more broadband and efficient the light-harvesting process is.

C. Field enhancement on convex and concave rough surfaces

Apart from the distinct absorption behavior, the convex and concave rough surfaces can also create a considerable field enhancement which can be exploited for surface-enhanced Raman scattering. In this section, the dependence of Raman signal enhancements on the contact angle between the asperities and the metal surface and on the incident light polarization will be discussed in detail.

By injecting the expression of x, y, p_x, and p_y [Eqs. (1) and (4)] into Eqs. (25) and (26), the potential can be expressed in the transformed frame:

$$\phi'^{\text{sca}}(x',y') = -\frac{a}{4}\Big[\big[-i\Gamma_y E_y'^{\text{inc}} + \text{sgn}(x')\Gamma_x E_x'^{\text{inc}}\big]e^{-f(\alpha,\theta)L(x',y')} + \big[-i\Lambda_y E_y'^{\text{inc}} + \text{sgn}(x')\Lambda_x E_x'^{\text{inc}}\big]e^{f(\alpha,\theta)L(x',y')}\Big]e^{if(\alpha,\theta)K(x',y')},$$

(31)

$$\phi'^{\text{m}}(x',y') = -\frac{a}{2(\varepsilon+1)}\Big[\big[-i\Theta_y E_y'^{\text{inc}} + \text{sgn}(x')\Theta_x E_x'^{\text{inc}}\big]e^{-f(\alpha,\theta)L(x',y')}$$
$$+ \big[-i\Omega_y E_y'^{\text{inc}} + \text{sgn}(x')\Omega_x E_x'^{\text{inc}}\big]e^{f(\alpha,\theta)L(x',y')}\Big]e^{if(\alpha,\theta)K(x',y')},$$

(32)

where

$$K(x',y') = \frac{1}{4\pi}\text{sgn}(x')\ln\frac{(x'+a/2)^2 + y'^2}{(x'-a/2)^2 + y'^2}, \qquad L(x',y') = \frac{1}{2\pi}\arctan\left(\frac{ay'}{x'^2 + y'^2 - a^2/4}\right).$$

Then the electric field $E'(x',y')$ can be easily deduced from the potential (e.g., $E'_{u'} = \partial\phi'/\partial u'$, where $u' = x',y'$)

$$E_{x'}'^{\text{sca}}(x',y') = \frac{af(\alpha,\theta)}{4}e^{if(\alpha,\theta)K(x',y')}\Big\{L(x',y')\frac{\partial L}{\partial x'}\big[\big[i\Gamma_y E_y'^{\text{inc}} - \text{sgn}(x')\Gamma_x E_x'^{\text{inc}}\big]e^{-f(\alpha,\theta)L(x',y')}$$
$$+ \big[i\Lambda_y E_y'^{\text{inc}} - \text{sgn}(x')\Lambda_x E_x'^{\text{inc'}}\big]e^{f(\alpha,\theta)L(x',y')}\big] + K(x',y')\frac{\partial K}{\partial x'}\big[\big[i\Gamma_y E_y'^{\text{inc}} + i\,\text{sgn}(x')\Gamma_x E_x'^{\text{inc}}\big]e^{-f(\alpha,\theta)L(x',y')}$$
$$+ \big[i\Lambda_y E_y'^{\text{inc}} + i\,\text{sgn}(x')\Lambda_x E_x'^{\text{inc}}\big]e^{f(\alpha,\theta)L(x',y')}\big]\Big\},$$

(33)

$$E_{y'}'^{\text{sca}}(x',y') = \frac{af(\alpha,\theta)}{4}e^{if(\alpha,\theta)K(x',y')}\Big\{L(x',y')\frac{\partial L}{\partial y'}\big[\big[i\Gamma_y E_y'^{\text{inc'}} - \text{sgn}(x')\Gamma_x E_x'^{\text{inc'}}\big]e^{-f(\alpha,\theta)L(x',y')}$$
$$+ \big[i\Lambda_y E_y'^{\text{inc'}} - \text{sgn}(x')\Lambda_x E_x'^{\text{inc'}}\big]e^{f(\alpha,\theta)L(x',y')}\big] + K(x',y')\frac{\partial K}{\partial y'}\big[\big[i\Gamma_y E_y'^{\text{inc'}} + i\,\text{sgn}(x')\Gamma_x E_x'^{\text{inc'}}\big]e^{-f(\alpha,\theta)L(x',y')}$$
$$+ \big[i\Lambda_y E_y'^{\text{inc'}} + i\,\text{sgn}(x')\Lambda_x E_x'^{\text{inc'}}\big]e^{f(\alpha,\theta)L(x',y')}\big]\Big\},$$

(34)

$$E_{x'}^{'m}(x',y') = \frac{af(\alpha,\theta)}{2(\varepsilon+1)}e^{if(\alpha,\theta)K(x',y')}\left\{L(x',y')\frac{\partial L}{\partial x'}\left[[i\Theta_y E_y^{inc'} - \text{sgn}(x')\Theta_x E_x^{inc'}]e^{-f(\alpha,\theta)L(x',y')}\right.\right.$$

$$+\left[i\Omega_y E_y^{inc'} - \text{sgn}(x')\Omega_x E_x^{inc'}\right]e^{f(\alpha,\theta)L(x',y')}\right] + K(x',y')\frac{\partial K}{\partial x'}\left[[i\Theta_y E_y^{inc'} + i\,\text{sgn}(x')\Theta_x E_x^{inc'}]e^{-f(\alpha,\theta)L(x',y')}\right.$$

$$+\left.\left.\left[i\Omega_y E_y^{inc'} + i\,\text{sgn}(x')\Omega_x E_x^{inc'}\right]e^{f(\alpha,\theta)L(x',y')}\right]\right\}, \tag{35}$$

$$E_{y'}^{'m}(x',y') = \frac{af(\alpha,\theta)}{2(\varepsilon+1)}e^{if(\alpha,\theta)K(x',y')}\left\{L(x',y')\frac{\partial L}{\partial y'}\left[[i\Theta_y E_y^{inc'} - \text{sgn}(x')\Theta_x E_x^{inc'}]e^{-f(\alpha,\theta)L(x',y')}\right.\right.$$

$$+\left[i\Omega_y E_y^{inc'} - \text{sgn}(x')\Omega_x E_x^{inc'}\right]e^{f(\alpha,\theta)L(x',y')}\right] + K(x',y')\frac{\partial K}{\partial y'}\left[[i\Theta_y E_y^{inc'} + i\,\text{sgn}(x')\Theta_x E_x^{inc'}]e^{-f(\alpha,\theta)L(x',y')}\right.$$

$$+\left.\left.\left[i\Omega_y E_y^{inc'} + i\,\text{sgn}(x')\Omega_x E_x^{inc'}\right]e^{f(\alpha,\theta)L(x',y')}\right]\right\}. \tag{36}$$

Figure 5 displays our analytical calculation of the normalized electric-field distributions for silver surfaces with a half-cylinder-shaped protuberance/indentation (e.g., $\theta = 90°$) at the cutoff and surface-plasmon frequencies. The surface-plasmon modes in the transformed frame are excited at the middle point of the protrusion/indentation surface, and then propagate towards the two singularities of the structure. In this process, SPPs are compressed and energy accumulates at the vicinities of the two singularities. Thus, the field enhancement depends on a balance between the dissipation losses and the compression of surface plasmons. From Figs. 5(a1) and 5(a2), we see that at the cutoff frequency ω_c, the energy is highly confined around the two apexes of the structures and the field is relatively small on the rest of the metal surface, indicating that the surface plasmons reach the two apexes
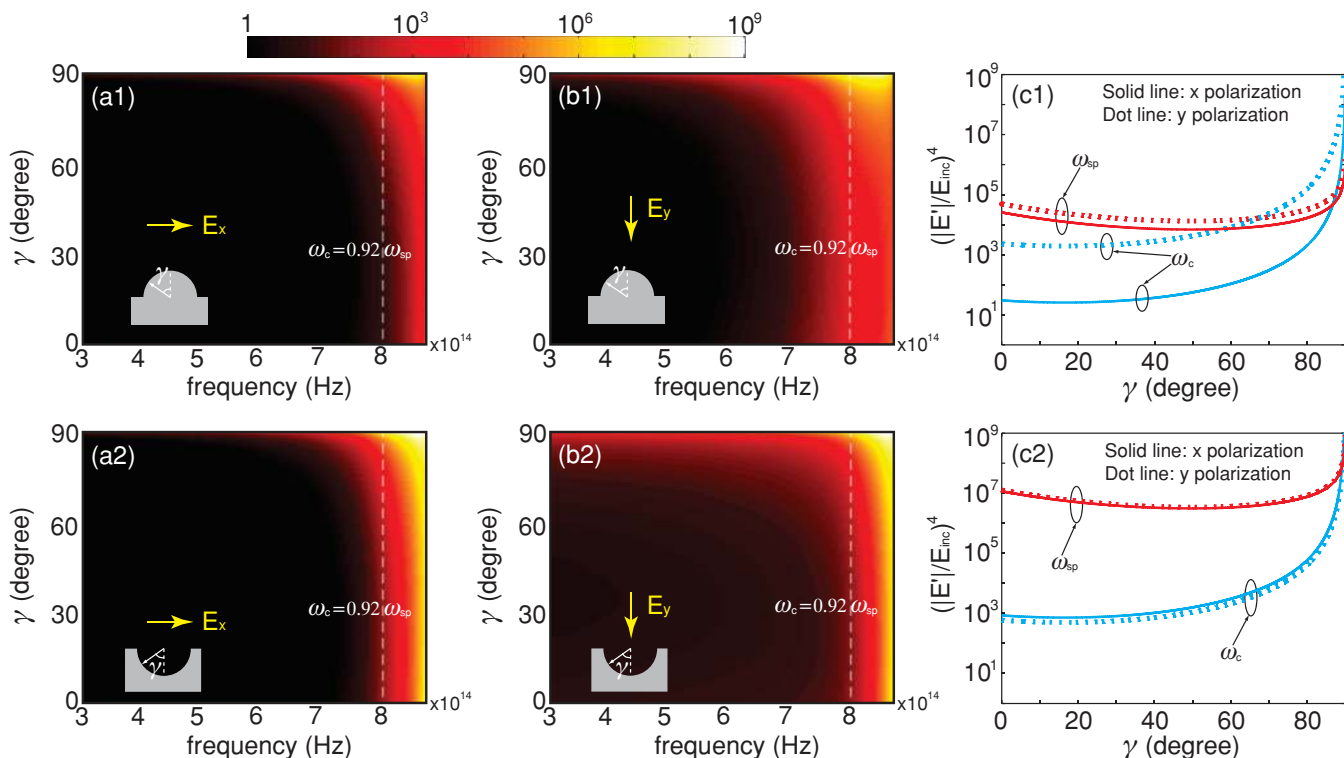

FIG. 6. (Color online) EM enhancements of Raman signals evaluated along the surfaces of the protuberance (upper panels) and indentation (bottom panels) when $\theta = 9°$. (a1) and (a2) show the results for x-polarized illumination, while (b1) and (b2) correspond to y-polarized illumination. In (c1) and (c2) we plot the Raman signal enhancement as a function of the angle γ at two specific frequencies, namely, 810 THz (the cutoff frequency ω_c) and 884 THz (the surface-plasmon frequency ω_{sp}). Here the angle γ is defined in the insets of (a1), (b1), (a2), and (b2).
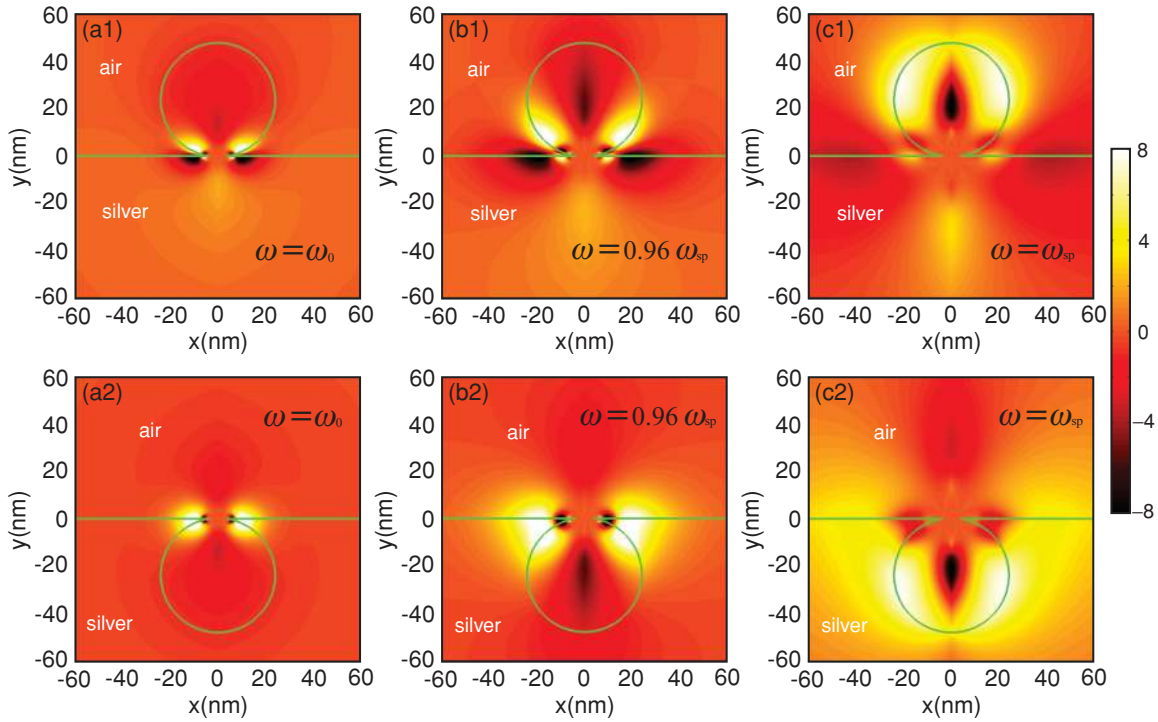
FIG. 7. (Color online) The real part of the normalized electric field E'/E'_{inc} for convex (upper panels) and concave (bottom panels) rough silver surfaces at different frequencies when $\theta = 9°$. (a1)/(a2) $\omega = \omega_0 = 790$ THz; (b1)/(b2) $\omega = 0.96\omega_{sp} = 850$ THz; and (c1)/(c2) $\omega = \omega_{sp} = 884$ THz.
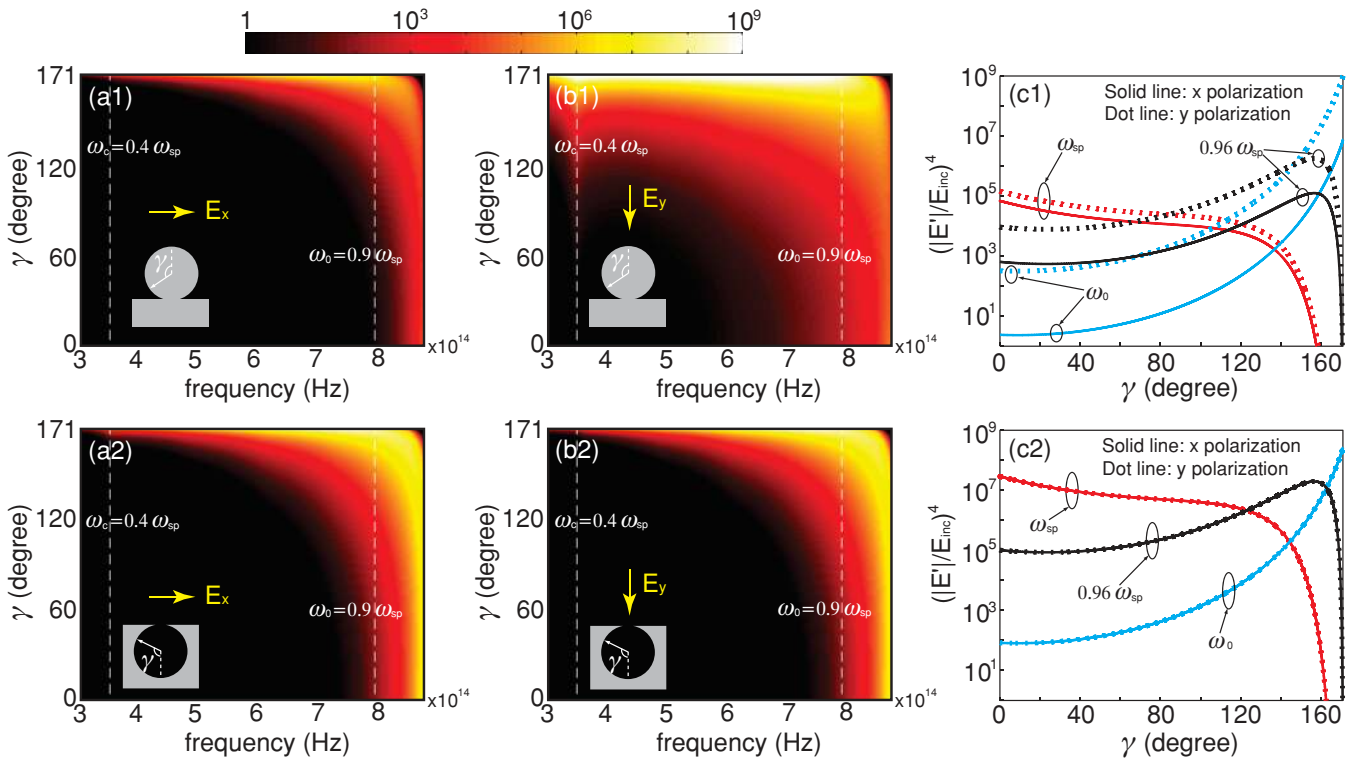

FIG. 8. (Color online) EM enhancements of Raman signals evaluated along the surfaces of the protuberance (upper panels) and indentation (bottom panels) when $\theta = 9°$. (a1) and (a2) show the results for x-polarized illumination, while (b1) and (b2) correspond to y-polarized illumination. In (c1) and (c2) we plot the Raman signal enhancement as a function of the angle γ at three specific frequencies, namely, 790 THz (the critical frequency ω_0), 850 THz ($\omega = 0.96\omega_{sp}$), and 884 THz (surface-plasmon frequency ω_{sp}). Here the γ angle is defined in the insets of (a1), (b1), (a2), and (b2).

before being absorbed. On the contrary, Figs. 5(b1) and 5(b2) show that at the surface-plasmon frequency ω_{sp}, the electric field vanishes at the singularities: the dissipation losses in the metal are important around ω_{sp} and the surface plasmons are absorbed before reaching the apexes. However, the efficient coupling of the incoming light to SPPs at this frequency also results in a relatively large field enhancement over the whole protrusion/indentation surface.

Figure 6 shows the Raman signal enhancement (calculated as $|E'|^4$) along the protrusion/indentation surface for different frequencies. From Figs. 6(a1) and 6(b1), we see that a convex rough surface exhibits different EM responses according to the polarization of the incident field. However, this difference seems to diminish as the frequency increases. For instance, Fig. 6 (c1) shows that at the surface-plasmon frequency ω_{sp} the solid and dotted lines (corresponding to the EM enhancements under x- and y-polarized illumination) nearly overlap.

Another interesting result of our calculation is the comparison between the convex and concave rough surfaces. Although the analysis in the former section [see Figs. 4(b1) and 4(b2)] shows that for a y-polarized incident field the convex rough surface can harvest light energy more efficiently than the concave one, it does not necessarily mean that the convex rough surface can induce larger Raman signal enhancements. For instance, at ω_{sp}, the overall Raman signal enhancement on the convex rough surface is about 10^5 [see Fig. 6(c1)], whereas for the concave rough surface, the EM enhancements in the Raman signal reaches 10^7 [see Fig. 6(c2)]. This result can be understood by inspecting the field distributions in Fig. 5. For the convex surfaces [Figs. 5(a1) and 5(b1)], a large amount of the energy is confined inside the metal, while for the concave ones [Figs. 5(a2) and 5(b2)], most of the energy remains in the air. Therefore, the concave metal surfaces show a poorer light-harvesting efficiency but a better Raman-scattering response, compared with the convex ones.

To study the influence of the contact angle $\theta = 9°$, we have also calculated the field enhancements for silver surfaces with different protuberances/indentations. Figure 7 depicts the normalized electric-field distributions E'/E'_{inc} at three different frequencies (790, 850, and 884 THz) for the convex and concave rough surfaces when $\theta = 9°$. The corresponding Raman signal enhancements along the protuberance/indentation surface are shown in Fig. 8. In contrast to the case discussed above (where $\theta = 90°$), a critical frequency ω_0 emerges in this case. Figures 8(a1), 8(a2), 8(b1), and 8(b2) show that below ω_0 surface-plasmon modes are highly confined in the vicinitiy of the singularities. On the contrary, above ω_0 the electric field vanishes at the singularities.

As the frequency increases, the location of the maximum of the Raman signal enhancement moves continuously from the singularity (where $\gamma = 171°$) to the middle point of the protrusion/indentation surface (where $\gamma = 0°$), which can be seen from Figs. 8(c1) and 8(c2). The comparison between Figs. 6 and 8 highlights the importance of the contact angle between the asperities and the metal surface. A small contact angle implies a larger and more broadband SERS response.

It is worth noticing that the Raman signal enhancement obtained at the apexes of the structures may be unrealistic in practice. This is because at such small-length scales, continuum electrodynamics is no longer valid[19] and shorter electron scattering lengths close to the apexes will play an essential role, especially for small contact angles. In this case, the bulk permittivity of metals has to be corrected to take into account this effect. This will increase the imaginary part of the dielectric function and will reduce the field enhancement at the apexes as compared to our analytical prediction.

V. CONCLUSION

In conclusion, we have presented a transformation optics approach to investigate systematically two conventional plasmonic structures, which are widely used in SERS experiments. An analytical relationship has been established between a canonical metallodielectric system and the two examined structures. Compared with traditional computational methods, our analytical approach does not require an implementation of adaptive meshes around the singularities (e.g., sharp edges or surface protrusions), thereby allowing a more comprehensive understanding of surface-plasmon modes responsible for SERS responses. The diverse EM characteristics of the structures in different frequency ranges have been studied quantitatively in terms of the contact angle between the asperities and the metal surface and of the incident light polarization. Metal surfaces with a cylindrical indentation are found to exhibit stronger Raman signal enhancements than those with a complementary protrusion. Moreover, a small contact angle between the asperities and the metal surface greatly improves the bandwidth and the efficiency of the SERS process. We believe that analytical approaches, such as the one considered in this paper, give a unique insight into the EM mechanism in SERS.

*Present address: Institut Langevin, ESPCI Paris Tech, CNRS UMR 7587, 10 rue Vauquelin, 75005 Paris, France; alexandre.aubry@espci.fr.

[1] M. Fleischmann, P. J. Hendra, and A. J. McQuillan, Chem. Phys. Lett. **26**, 163 (1974).

[2] M. G. Albrecht and J. A. Creighton, J. Am. Chem. Soc. **99**, 5215 (1977).

[3] M. Moskovits, Rev. Mod. Phys. **57**, 783 (1985).

[4] S. M. Nie and S. R. Emory, Science **275**, 1102 (1997).

[5] K. Kneipp, Y. Wang, H. Kneipp, L. T. Perelman, I. Itzkan, R. R. Dasari, and M. S. Feld, Phys. Rev. Lett. **78**, 1667 (1997).

[6] J. B. Jackson and N. J. Halas, Proc. Natl. Acad. Sci. USA **101**, 17930 (2004).

[7] J. J. Baumberg, T. A. Kelf, Y. Sugawara, S. Cintra, M. E. Abdelsalam, P. N. Bartlett, and A. E. Russell, Nano Lett. **5**, 2262 (2005).

[8] H. Ko, S. Singamaneni, and V. V. Tsukruk, Small **4**, 1576 (2008).

[9] J. N. Anker, W. P. Hall, O. Lyandres, N. C. Shah, J. Zhao, and R. P. Van Duyne, Nat. Mater. **7**, 442 (2008).

[10] F. J. García-Vidal and J. B. Pendry, Phys. Rev. Lett. **77**, 1163 (1996).

[11] F. J. García-Vidal, J. M. Pitarke, and J. B. Pendry, Phys. Rev. B **58**, 6783 (1998).

[12] J. A. Sánchez-Gil and J. V. García-Ramos, J. Chem. Phys. **108**, 317 (1998).

[13] J. A. Sánchez-Gil and A. A. Maradudin, Phys. Rev. B **60**, 8359 (1999).

[14] I. V. Novikov and A. A. Maradudin, Phys. Rev. B **66**, 035403 (2002).

[15] J. A. Sánchez-Gil, J. V. García-Ramos, and E. R. Méndez, Phys. Rev. B **62**, 10515 (2000).

[16] H. Xu, J. Aizpurua, M. Käll, and P. Apell, Phys. Rev. E **62**, 4318 (2000).

[17] J. P. Kottmann, O. J. F. Martin, D. R. Smith, and S. Schultz, New J. Phys. **2**, 27 (2000).

[18] J. P. Kottmann and O. J. F. Martin, Opt. Express **8**, 655 (2001).

[19] E. Hao and G. C. Schatz, J. Chem. Phys. **120**, 357 (2004).

[20] R. J. C. Brown, J. Wang, and M. J. T. Milton, J. Nanomater. **2007**, 12086 (2007).

[21] V. Giannini, J. A. Sánchez-Gil, J. V. García-Ramos, and E. R. Méndez, J. Chem. Phys. **127**, 044702 (2007).

[22] Z. B. Wang, B. S. Luk'yanchuk, W. Guo, S. P. Edwardson, D. J. Whitehead, L. Li, Z. Liu, and K. G. Watkins, J. Chem. Phys. **128**, 094705 (2008).

[23] A. J. Ward and J. B. Pendry, J. Mod. Opt. **43**, 773 (1996).

[24] J. B. Pendry, D. Schurig, and D. R. Smith, Science **312**, 1780 (2006).

[25] A. Aubry, D. Y. Lei, A. I. Fernandez-Dominguez, Y. Sonnefraud, S. A. Maier, and J. B. Pendry, Nano Lett. **10**, 2574 (2010).

[26] Y. Luo, J. B. Pendry, and A. Aubry, Nano Lett. **10**, 4186 (2010).

[27] Detailed analysis on the approximate solution to the surface-plasmon dispersion relation can be found in the supporting materials of Ref. 26 at [http://pubs.acs.org/doi/suppl/10.1021/nl102498s].

[28] E. D. Palik, *Handbook of Optical Constants of Solids* (Academic, New York, 1991), Vol. II.

[29] A. Aubry, D. Y. Lei, S. A. Maier, and J. B. Pendry, Phys. Rev. B **82**, 125430 (2010).

[30] A. Aubry, D. Y. Lei, S. A. Maier, and J. B. Pendry, Phys. Rev. B **82**, 205109 (2010).

[31] J. Lindhardt, Kgl. Danske Videnskab. Selskab. Mat.-Fys. Medd. **28**, No. 8 (1954).

[32] J. Zuloaga, E. Prodan, and P. Nordlander, Nano Lett. **9**, 887 (2009).

[33] G. W. Ford and W. H. Weber, Phys. Rep. **113**, 195 (1984).

[34] S. Enoch, R. Quidant, and G. Badenes, Opt. Express **12**, 3422 (2004).

[35] P. Nordlander, C. Oubre, E. Prodan, K. Li, and M. I. Stockman, Nano Lett. **4**, 899 (2004).

[36] L. A. Sweatlock, S. A. Maier, H. A. Atwater, J. J. Penninkhof, and A. Polman, Phys. Rev. B **71**, 235408 (2005).

[37] I. Romero, J. Aizpurua, G. W. Bryant, and F. J. García De Abajo, Opt. Express **14**, 9988 (2006).

[38] A. Aubry, D. Y. Lei, S. A. Maier, and J. B. Pendry, Phys. Rev. Lett. **105**, 233901 (2010).